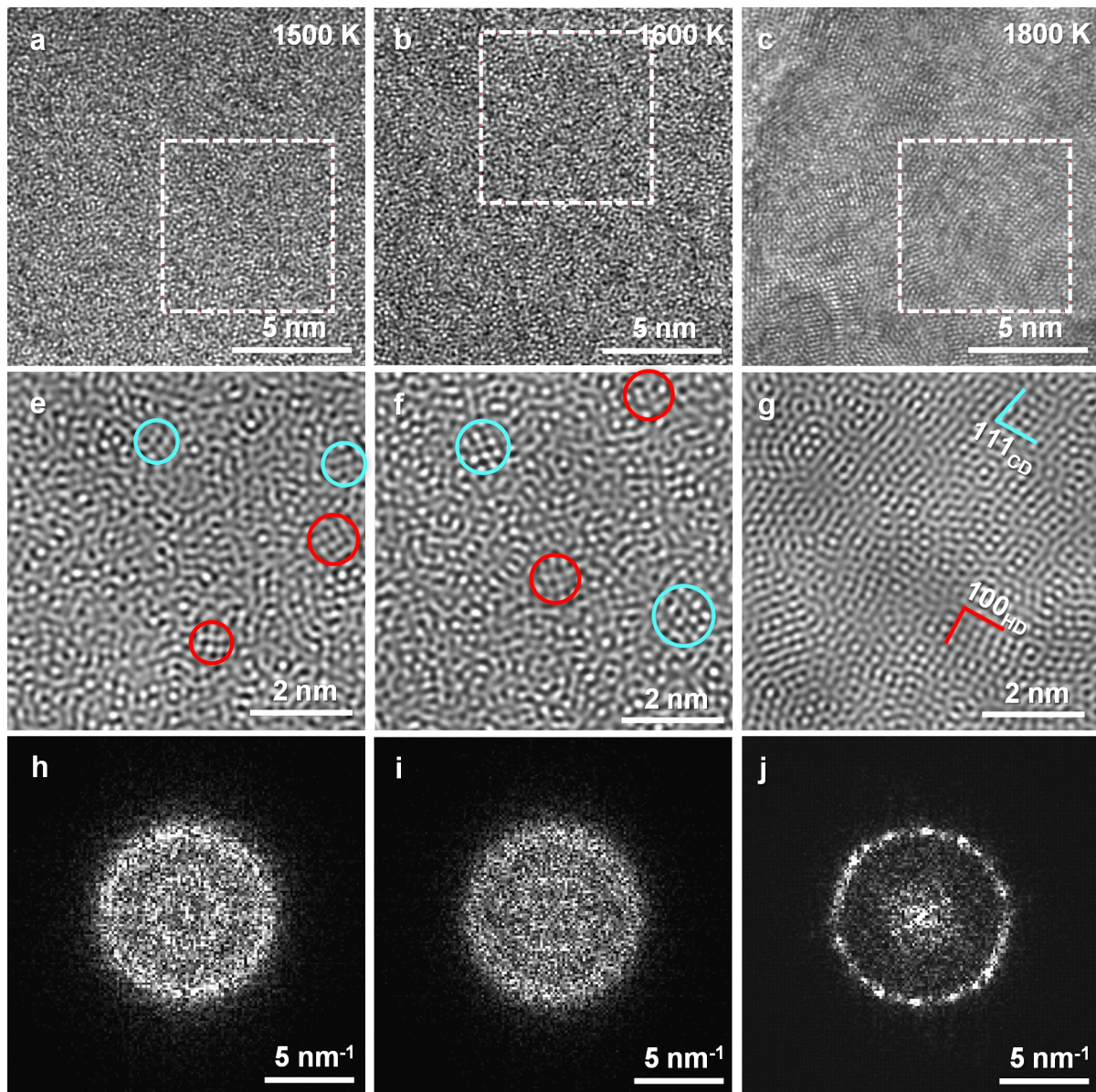


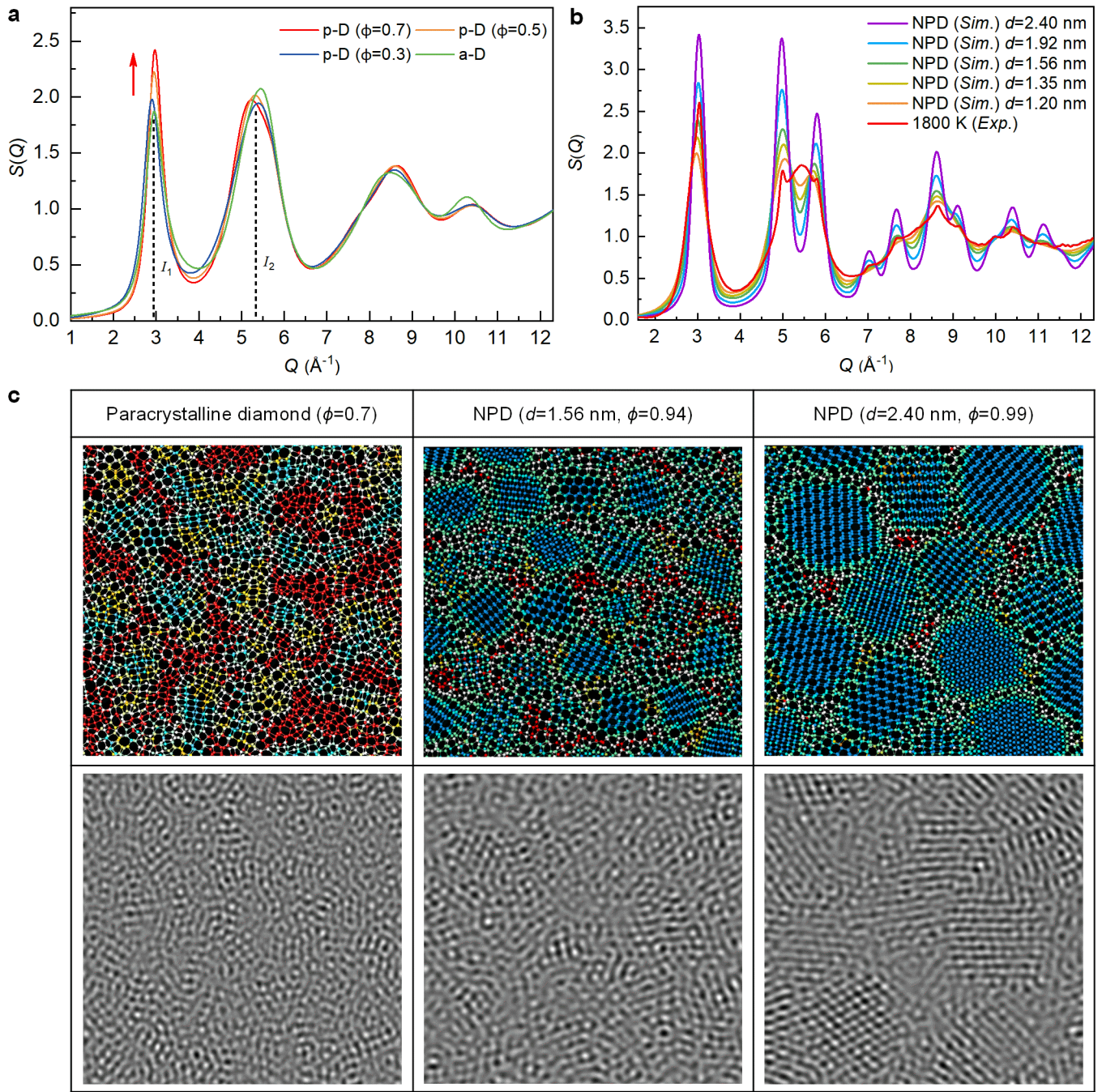
Extended Data Fig. 1 | XRD patterns, Raman spectra, fluorescence spectra, and EELS in the low-loss region of the recovered samples. **a**, XRD patterns of samples synthesized from different precursors: C_{60} (top), type-1 glassy carbon (middle), and carbon onion (bottom) at 30 GPa and 1400–1800 K, respectively. At 1800 K, the appearance of weak Bragg diffraction peaks indicates nano-crystallization in the non-crystalline diamond formed from C_{60} . At 1600 K, fully sp^3 -bonded p-D was identified. By contrast, in cases of using type-1 glassy carbon and carbon onion as the starting material, crystallization precedes the complete conversion of sp^2 to sp^3 carbon at 30 GPa and 1400–1600 K, preempting the formation of fully sp^3 -bonded paracrystalline diamond. The experiments demonstrate the importance of the structure of the starting material in the formation pathway of p-D. **b**, Visible Raman (532 nm) spectrum of the sample recovered at 30 GPa and 1400 K, with background removed. The broadened Raman peak can be fit with a D peak at 1378 cm^{-1} and a G peak at 1556 cm^{-1} . The peak intensity ratio of I_D/I_G is 0.66 and the full width at half maximum (FWHM) of the G peak is 175 cm^{-1} . Similar to our work, the presence of sp^2 bonds results in a wide Raman peak between 1400 cm^{-1} and 1700 cm^{-1} in the visible Raman spectra of diamond-like carbon (DLC) films²⁷. **c**, Ultraviolet (UV) Raman

spectra of the samples recovered from 1400 and 1500 K, respectively. The strong peak at 1110 cm^{-1} in the UV Raman spectrum of the sample recovered at 30 GPa and 1400 K is attributed to the T peak caused by sp^3 bonds²⁷. Fitting the Raman profile yields a peak intensity ratio of I_T/I_G 0.91, which is higher than that of DLC films with 88% sp^3 bonds, indicating a higher concentration of sp^3 bonds in the sample²⁷. On the other hand, for the sample recovered from 1500 K, no obvious peaks are discernible in the UV Raman spectrum, indicating the absence of sp^2 bonds in the as-synthesized disordered carbon⁸. **d**, Fluorescence spectra (excitation wavelength of 532 nm) of the sample from 1600 K and type Ia diamond. A main fluorescence peak centered around 702 nm suggests the high background in the Raman spectra is due to a fluorescence effect. **e**, EELS in the low-loss region of diamond crystal, single-crystal graphite, and samples synthesized from C_{60} under 30 GPa and 1400–1500 K. Based on plasmon peak energy derived from low-loss EELS²⁸, the densities of the recovered samples at 1400–1600 K were calculated to be 3.11, 3.20, and 3.25 g/ cm^3 , respectively. Due to the presence of ~5.2% sp^2 carbon, the sample recovered from 1400 K has a lower density of 3.11 g/ cm^3 .



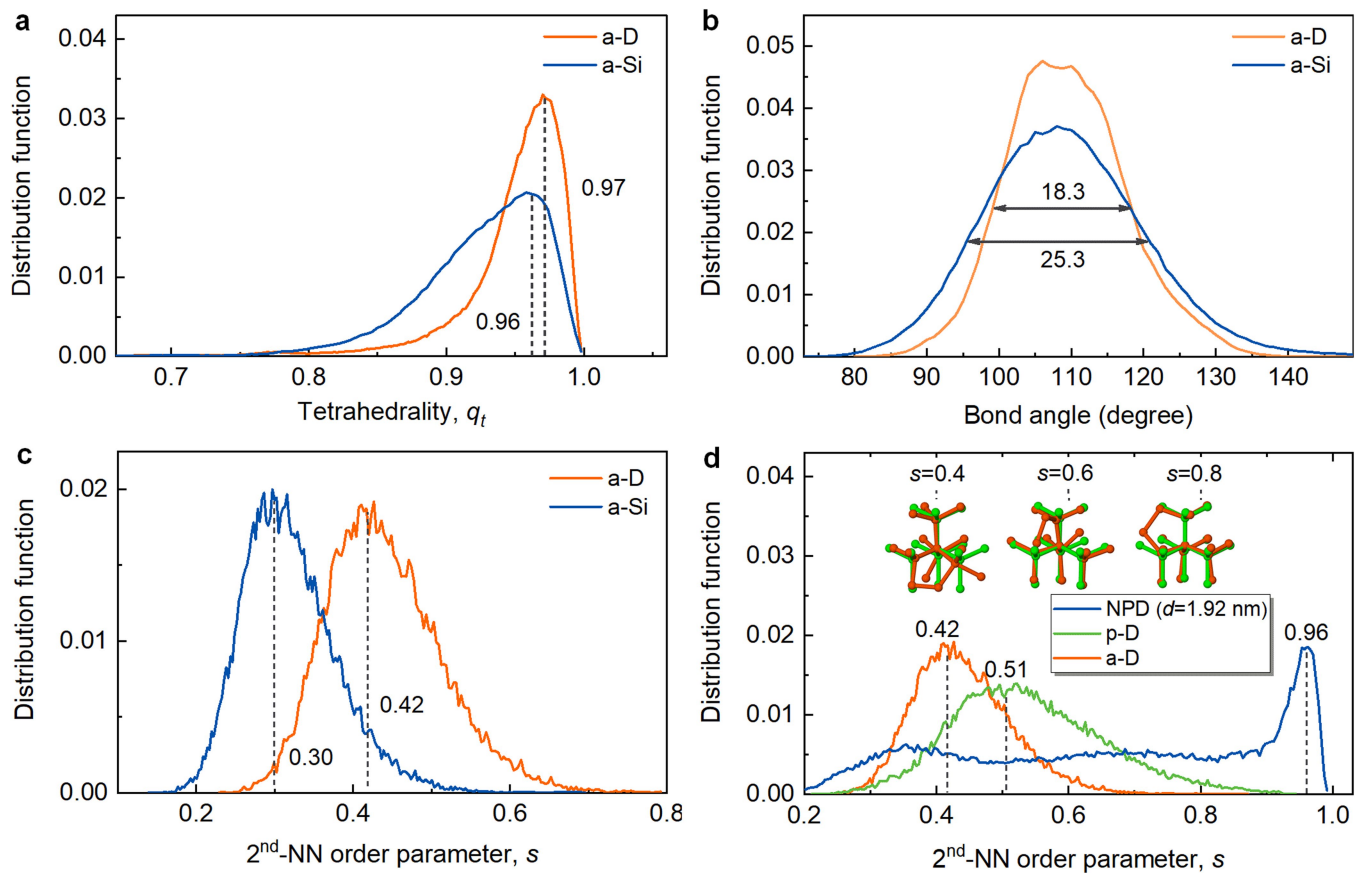
Extended Data Fig. 2 | HRTEM images of samples recovered at 30 GPa and different temperatures. a–c, Typical HRTEM images of samples synthesized at 30 GPa and 1500, 1600, and 1800 K, respectively. a–c and h–j, The inverse FFT images and FFT patterns corresponding to the areas marked by the white boxes ($7.0 \times 7.0 \text{ nm}^2$) in (a), (b), and (c), respectively. The cyan and yellow circles

in (e, f) indicate cubic- and hexagonal-like MRO clusters, respectively. In subfigure g, the lattice fringes marked with cyan and yellow solid lines indicate that nanosized cubic and hexagonal diamond crystallites are precipitated from the non-crystalline matrix at 1800 K.



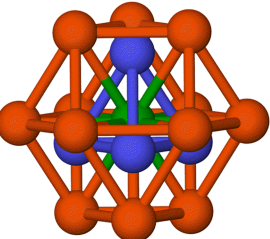
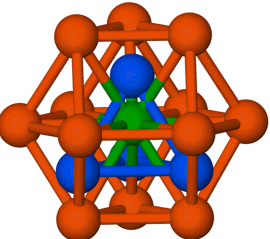
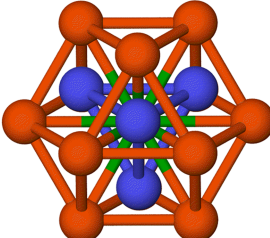
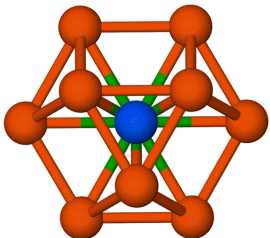
Extended Data Fig. 3 | Structure factor $S(Q)$, structural models, and simulated HRTEM images of simulated a-D, p-D with different fractions of paracrystallites, and NPD with different grain sizes. **a**, $S(Q)$ of simulated a-D and p-D with different fractions of paracrystallites. With increasing ϕ , the intensity of the first peak increases, and the position of the peak shifts to high- Q , which is consistent with the experimental observation that at higher annealing temperatures, the intensity of the first peak increases and the position moves to the right (from 2.89\AA^{-1} at 1200 K to 2.95\AA^{-1} at 1600 K , Fig. 3b in the main text). **b**, $S(Q)$ of simulated NPDs with different grain sizes, juxtaposed with that of the 1800 K sample from our experiment. For the

simulated NPD samples, the peak intensity decreases and the peak width broadens as the grain size is refined. Bragg peaks are clearly discernable for the samples with a grain size of 1.2 nm . Experimentally, the protruding diffraction peaks in the 1800 K sample corresponds exactly to the characteristic Bragg peaks of NPD, indicative of crystallization. **c**, In ultrafine NPD, the less-distorted “core” regions of the nanocrystals (blue spheres) are clearly seen. For NPD with $d=1.56\text{ nm}$, ϕ is estimated to be 94% , meaning 6% atoms are located at the interfaces and cannot be properly assigned to any of the crystalline grains.


Extended Data Fig. 4 | Short-range ordering of a-D, a-Si, p-D, and NPD.

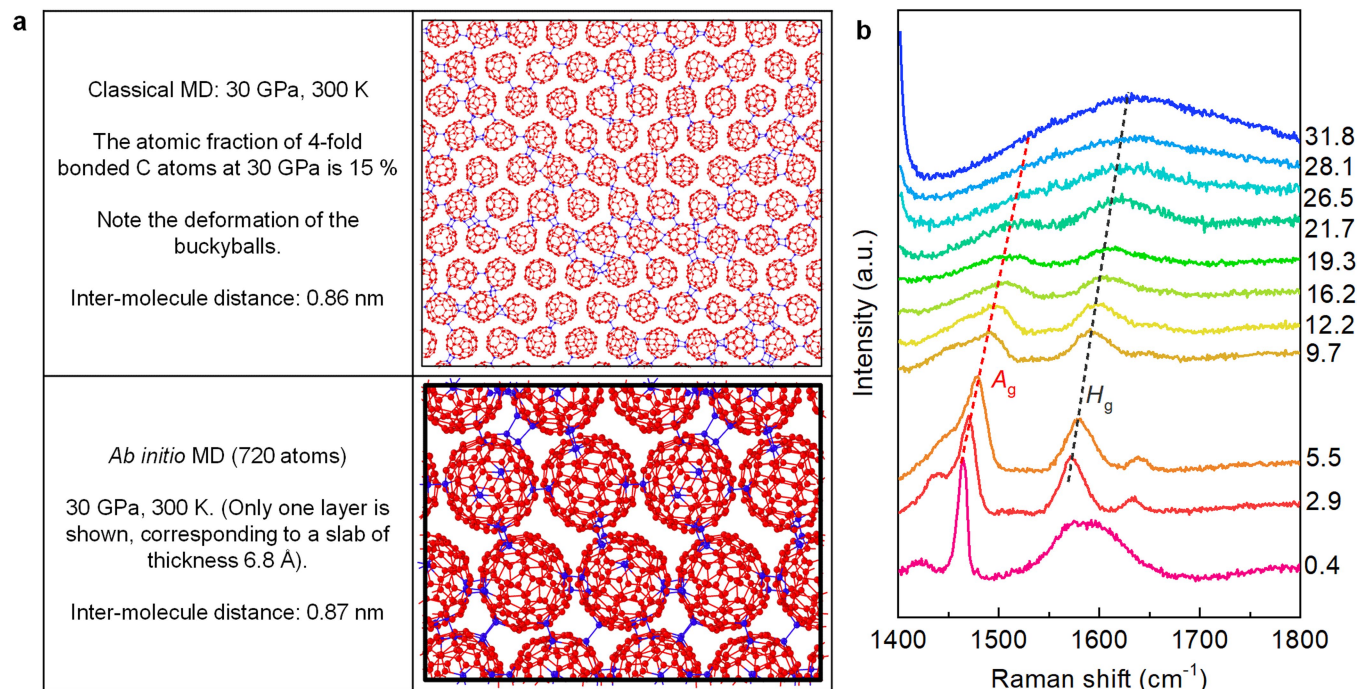
a, Distributions of tetrahedrality q_t for a-D and a-Si, both of which were obtained from the WWW bond-switching approach and further relaxed with *ab initio* MD. The tetrahedral order parameter q_t is defined as $q_t = 1 - \frac{3}{8} \sum_{i=1}^3 \sum_{j=i+1}^4 (\cos \theta_{ij} + 1/3)$, where θ_{ij} is the angle formed by two vectors pointing from the center silicon to two of its neighboring silicon atoms. The summation runs over all the combinations of the four nearest neighbors. The narrow distribution of a-D clearly indicates that a-D has a strong tetrahedral SRO than a-Si. **b**, Bond-angle distribution within the first atomic shell for a-D and a-Si. Compared with a-Si, a-D has a narrower bond-angle distribution. **c**, Distributions of the second-nearest-neighbour order parameter s of a-D and a-Si. The order parameter s measures the similarity of the local atomic environment (16 atoms) of a central atom with respect to perfect CD or HD lattice arrangements. The higher the s value, the less distortion of the local

cluster. Compared with a-Si, the distribution function of s for a-D shifts to high values with a centroid of 0.42, suggesting much enhanced SRO within the first two atomic shells in a-D. The high similarity of the local atomic environments between a-D and crystalline diamond stems from the strong directional sp^3 bonding of carbon, as evidenced from the narrower bond-angle distribution of a-D in comparison to that of a-Si. **d**, Distributions s of a-D, p-D, and NPD with a grain size of 1.92 nm. The inset atomic clusters illustrate the cluster configurations (red spheres) corresponding to their degree of similarity with the perfect CD lattice arrangement (green spheres). Paracrystalline diamond has a medium s value (0.51) between that of a-D and NPD, revealing crystalline ordering in p-D. It is worth noting that, for NPD with $d=1.92$ nm, the distribution spike at $s=0.96$ corresponds to interior atoms in nano-grains that are less distorted. Such atoms are absent in paracrystalline diamond, marking the distinction between p-D and NPD.

	Two atomic shell structure of CD (16 nearest neighbors)	Two atomic shell structure of HD (16 nearest neighbors)
Side view		
Top view		
Second-nearest-neighbor packing (red spheres)	FCC	HCP
CNA index	(421)	(422)

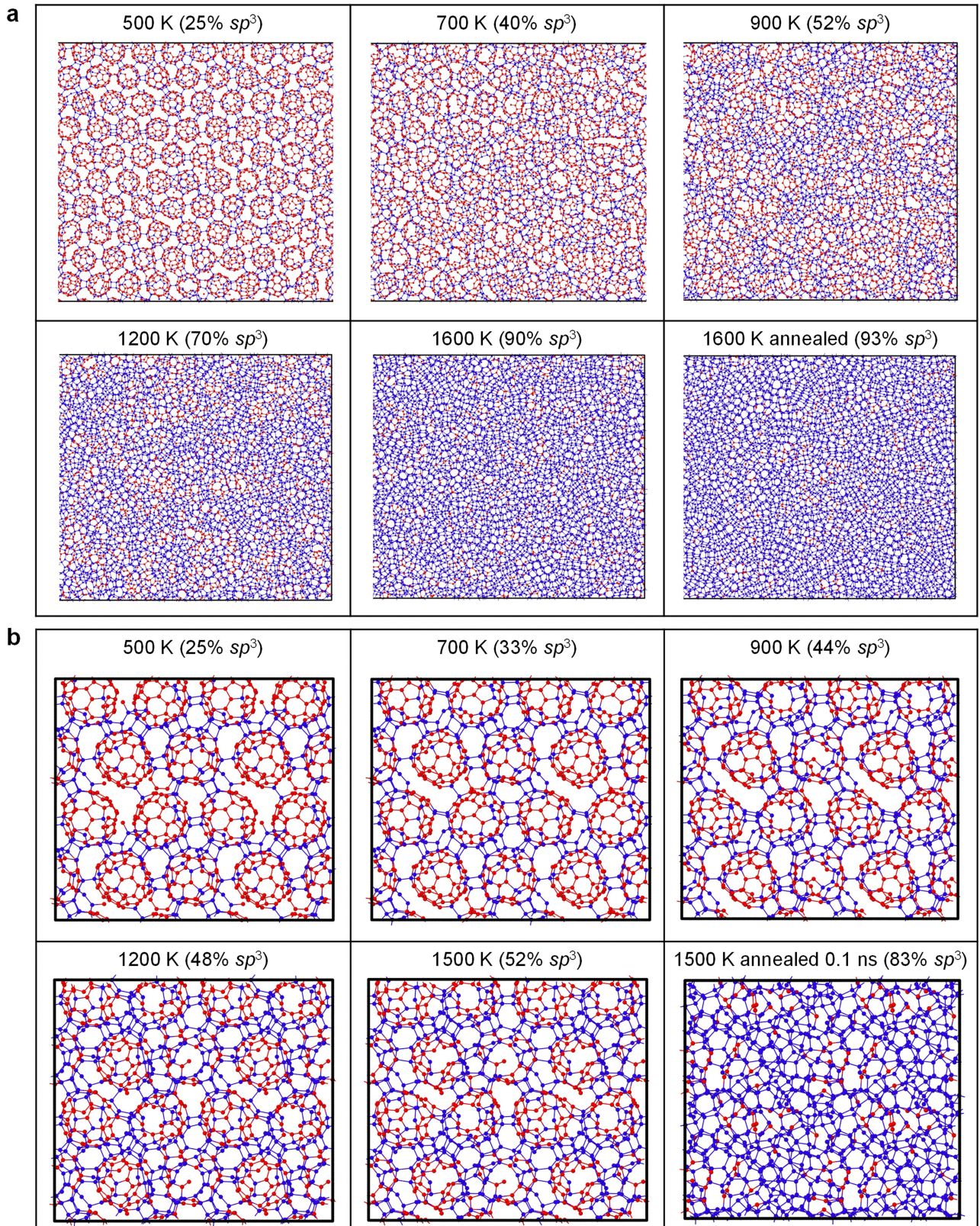
Extended Data Fig. 5 | Two atomic-shell structures (side and top views) of CD and HD (16 nearest neighbors) atomic packing. The 12 second nearest neighbors in CD and HD are arranged in the FCC and HCP packing modes, respectively.

Article



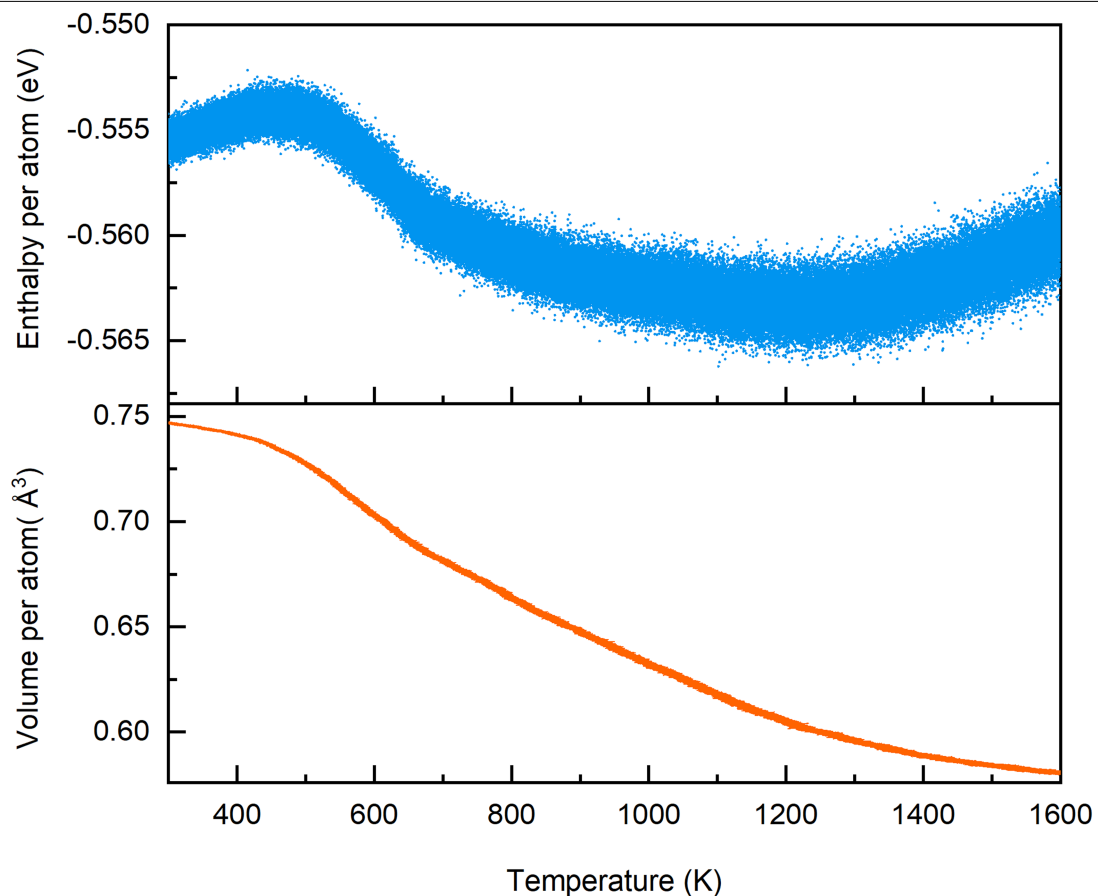
Extended Data Fig. 6 | Structural evolution of C_{60} under room-temperature compression. **a**, Structure model (Only one layer is shown) of C_{60} under 30 GPa and room temperature (300 K), obtained by classic and *ab initio* MD. Under high pressure (30 GPa), the inter-molecule distance reduces to 0.86 or 0.87 nm from 1.0 nm. During compression to 30 GPa at room temperature, the buckyballs are deformed and inter-buckyball bonding occurs by formation of four-fold (sp^3) bonds (15%). In this and the following figures, the atoms with sp^3 bonding are colored in blue. The fraction of sp^3 atoms was approximated by the number of 4-fold coordinated atoms within a cut off distance (in this work, $r_{cut}=1.85 \text{ \AA}$). We shall point out that, the sp^3 fraction calculated this way is slightly

underestimated in comparison to that calculated quantum-mechanically, e.g., with the maximally localized Wannier function (MLWF). **b**, *In situ* Raman spectra of C_{60} under compression (up to ~32 GPa) without pressure transmitting medium, with an excitation wavelength of 532 nm. With increasing pressure, the Raman peaks of the A_g mode corresponding to the breathing of totally symmetric vibrations and the H_g mode are gradually broadened with decreased intensity, suggesting a gradual decline of the symmetric environment of pristine C_{60} , associated with the polymerization of buckyballs⁶⁹ and the formation of sp^3 bonds⁷⁰, consistent with our theoretical results.



Extended Data Fig. 7 | MD simulation of fcc-C₆₀ heated to different temperatures at 30 GPa. **a**, Classic MD simulation of fcc-C₆₀, heating rate: 10^{10} K/s. The fraction of sp^3 bonds increase with increasing temperature. There is a percolation transition of sp^3 bonds at 500–800 K. Such a percolation transition corresponds to the polymerization of C₆₀ molecules. It should be pointed out that the fractions of sp^3 bonding were determined based on the criterion of

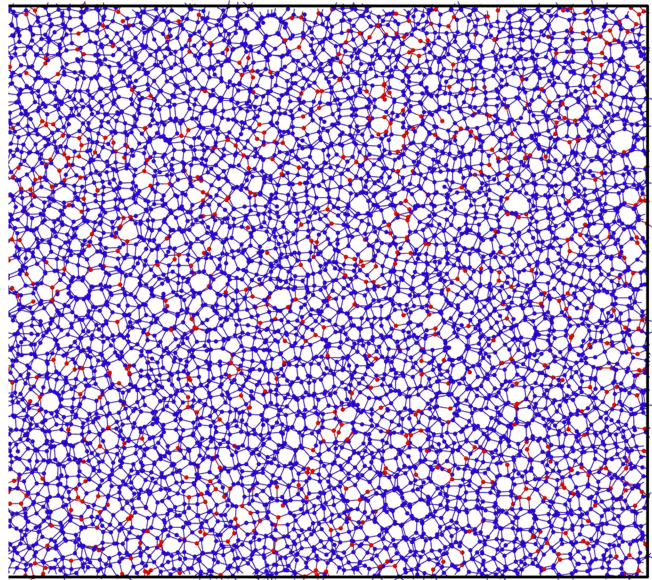
4-fold bonding within 1.85 Å, which may slightly underestimate the real sp^3 fraction of the sample by a few percent. **b**, *Ab initio* MD simulation of fcc-C₆₀ (720 atoms), heating rate: 2×10^{14} K/s. Similar to classic MD simulation, the fraction of sp^3 bonds increases with increasing temperature in *ab initio* MD. The simulation results validate what was observed in classical MD. Note the persistence of parallel sp^3 bonds at 900 K and 1200 K.



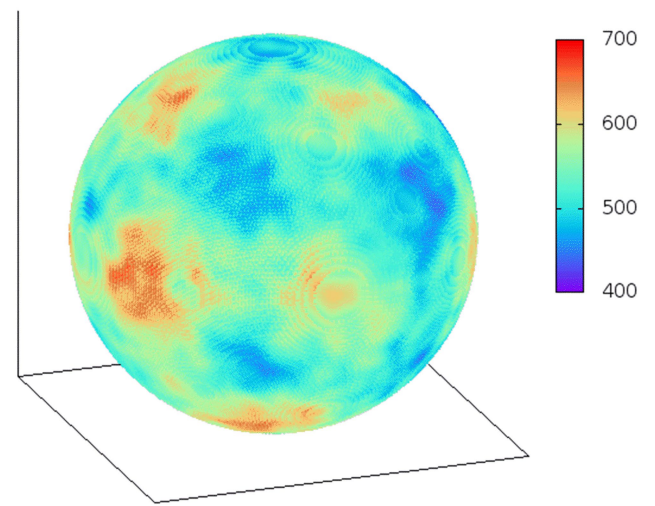
Extended Data Fig. 8 | Enthalpy and volume as a function of temperature during the heating treatment of C_{60} at 30 GPa. The decrease of enthalpy with increasing temperature (500–1250 K) indicates the main sp^2 - sp^3 transition (25% to 70% as shown in Extended Data Fig. 7a) occurs between 500 K and 1250 K,

accompanied by the densification of the material due to the formation of sp^3 bonding. The uprise of the enthalpy at temperatures below 500 K and above 1250 K is mainly due to the thermal effect.

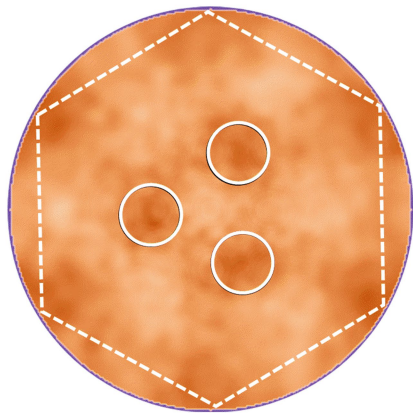
C_{60} heated to 1600K at 30 GPa



3D bond-orientational distribution function projected onto the unit sphere surface,
 $\phi(\hat{r})$

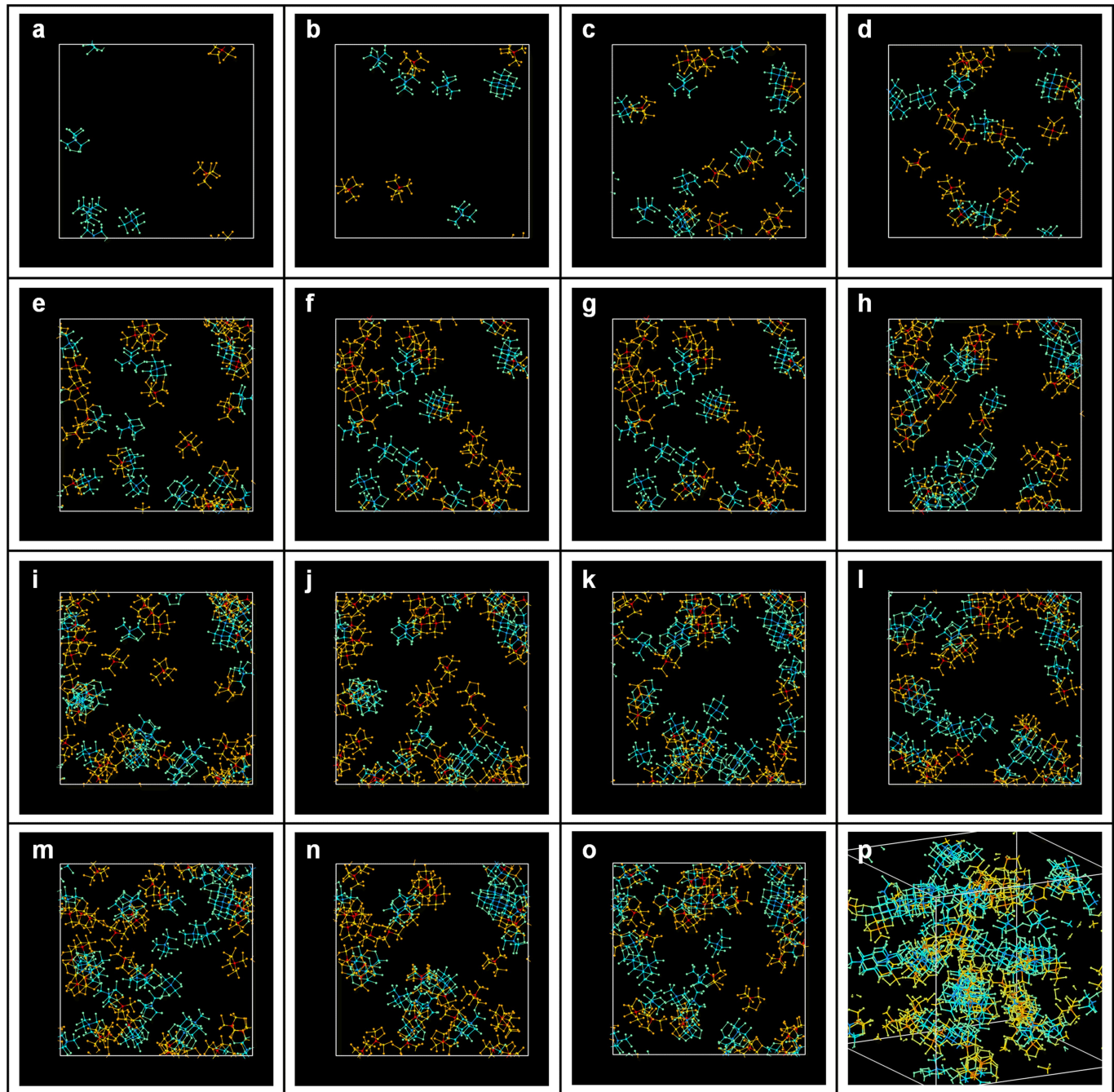


2D pole figure showing preferred bond orientations



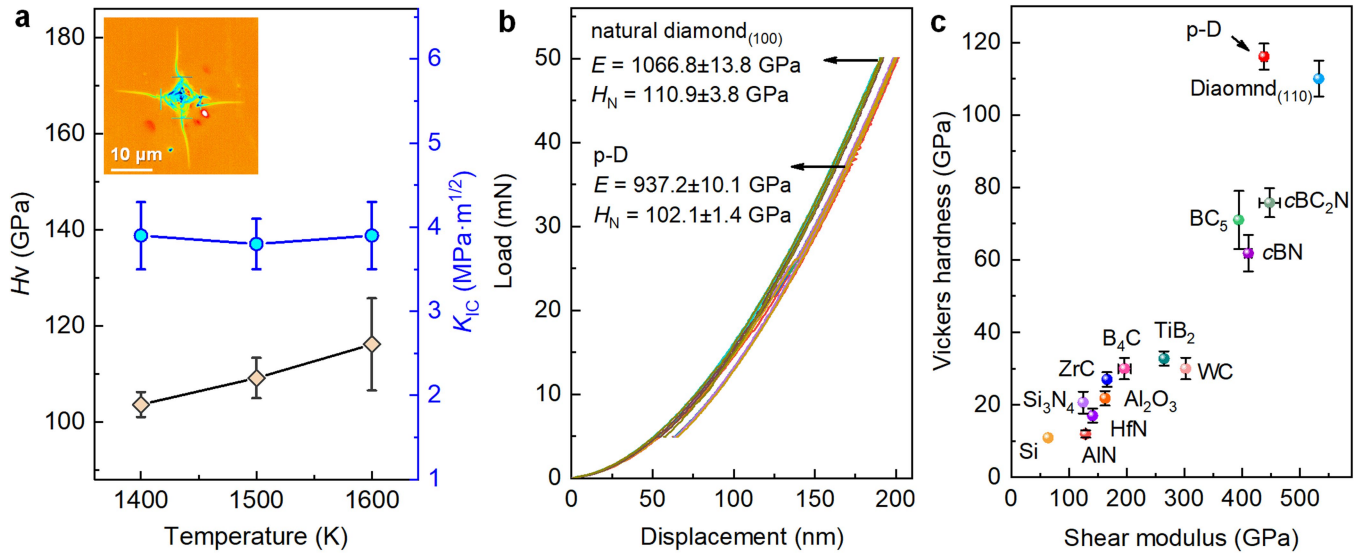
Extended Data Fig. 9 | Hidden orientational ordering of sp^3 bonds in compressed C_{60} . Top: Structure model of a-D obtained from C_{60} after 30 GPa and 1600 K without long-time isothermal annealing (Extended Data Fig. 7a). Middle: 3D bond-orientation distribution function projected onto the unit sphere surface. Bottom: Two-dimensional stereographic projection of the

bond-orientation function showing the pole figure of preferred bond orientations. The lines serve as a guide to the eye. Heterogeneous intensity distributions suggest that the sp^3 bonds in the as-obtained a-D have preferred orientations, inherited from the initial parallel sp^3 bonds in the early stage of polymerization.



Extended Data Fig. 10 | Classic MD simulation of the structural evolution of a-D during isothermal annealing at 1600 K and 30 GPa, 6400 atoms, up to 15 ns. Only the core atoms of the paracrystallites are shown. The paracrystallites marked by turquoise and gold have CD and HD-like structures, respectively. The fraction of paracrystallites increases with the annealing time (a–o, at a time interval of 1 ns per image). The last image (p) shows a 3D

configuration paracrystalline diamond with $\phi = 20\%$ obtained from brute-force classical MD. To further increase the volume fraction of p-D, we resorted to adiabatic-bias molecular dynamics and the final results are given in Fig. 3 of the main text. See Supplementary Video for the fluctuations of the paracrystallites.



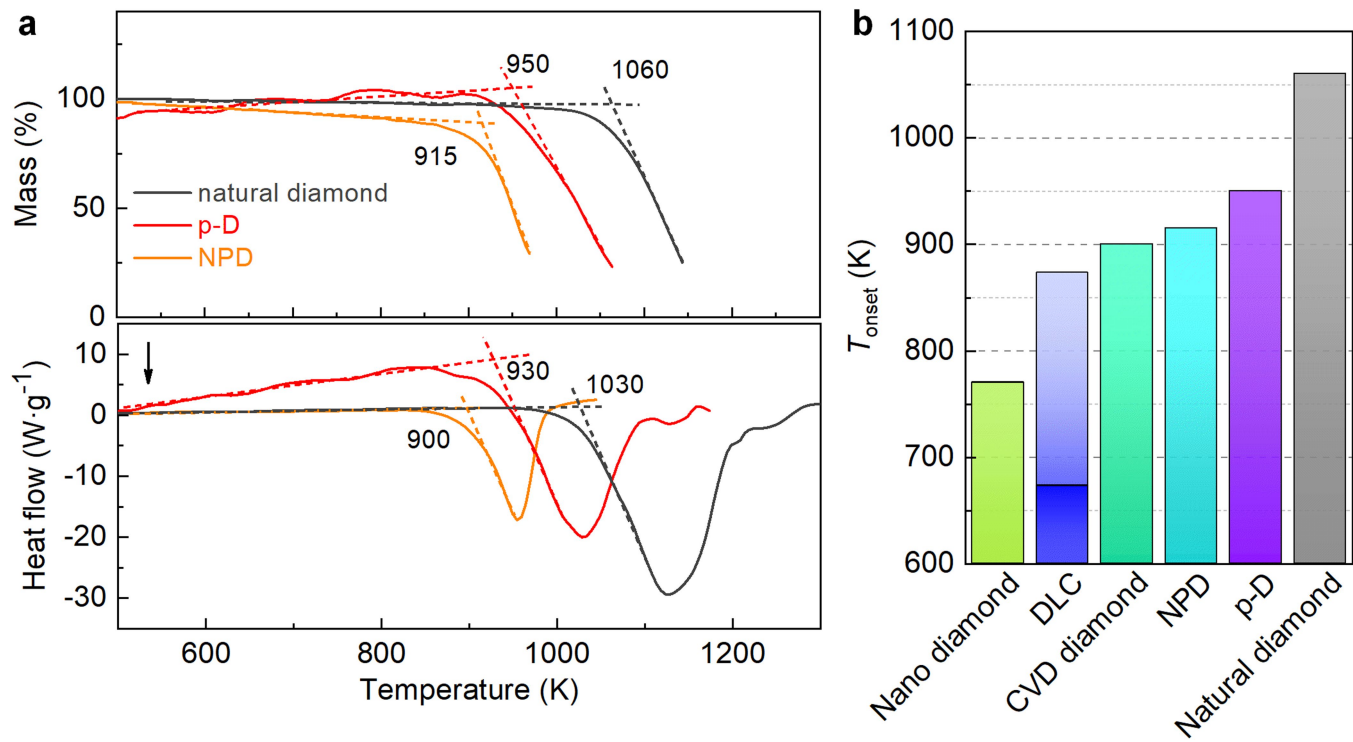
d	<i>sp</i> ³ carbon	Calculated hardness (GPa)	Experimental hardness H_V (GPa)
P-D	---	---	116
Diamond ^{42,46}	96	110 ₍₁₁₀₎ , 62 ₍₁₁₁₎	
Hexagonal diamond ⁷³	152	---	
Carbon Clathrates ⁷⁴	83.5	---	
NPD ^{39,41}	---	66-140 _{H_K}	
NTD ^{42,75}	200	200	

e		Young's modulus (GPa)	bulk modulus (GPa)
Diamond	Calculated	1162.7 ± 7.6 _[111]	427.9 ± 1.6
	Experimental ⁷⁶	1140.0 ± 1.0	441.8 ± 0.8
P-D	Calculated	952.5 ± 4.9	387.4 ± 2.7
	Experimental	937.2 ± 10.1	363.3 ± 3.9

Extended Data Fig. 11 | Mechanical properties of recovered samples.

a, Vickers hardness H_V and fracture toughness K_c of the samples recovered at 30 GPa and different temperatures, measured at 4.9 and 9.8 N, respectively. Inset: an optical image of the indentation of p-D recovered from 1600 K. **b**, Side-by-side comparison of the loading/unloading displacement curves of p-D recovered from 1600 K and natural diamond in the nanoindentation experiment. Inset: A table of nanoindentation hardness H_N and elastic modulus E obtained from different test points. **c**, Overview of shear modulus G versus Vickers hardness H_V for typical superhard ceramics^{42,46,71,72}. The shear modulus G (437.9 ± 4.7 GPa) and bulk modulus K (363.3 ± 3.9 GPa) was derived through

formulas $G = E/[2(1 + \mu)]$ and $K = E/[3(1 - 2\mu)]$, where the elastic modulus E (937.2 ± 10.1 GPa) was experimentally measured (shown in b) and μ is the Poisson's ratio (0.07) of diamond. Error bars in a and c indicate the standard deviations. **d**, Summary for the calculated and experimental hardness of typical *sp*³ carbons of p-D, diamond^{42,46}, hexagonal diamond⁷³, carbon clathrates⁷⁴, NPD^{39,41} and nanotwinned diamond (NTD)^{42,75}. **e**, Comparison of theoretical Young's modulus and bulk modulus of p-D and diamond⁷⁶. For the *ab initio* calculations, we used DFT-based *ab initio* modeling stated in the Methods section but with a smaller-sized p-D sample (240 atoms) derived from classical MD.



Extended Data Fig. 12 | Thermostability of p-D. **a**, Both thermogravimetry (TG) and DSC curves of p-D were measured in air at a heating rate of 5 K/min. **b**, Thermostability of p-D, compared with other superhard carbons^{47–49}.

Superhard (50–80 GPa) DLC films have a wide range of onset oxidation temperature (673–873 K), depending on the fraction of sp^3 bonds. The thermostability of p-D is superior to that of NPD ($d = 13 \text{ nm}$)⁴³.